Characterisation of an X-Ray Waveguide for use in Incoherent Imaging

KJ Tsanaktsidis

Supervised by Daniele Pelliccia and David Paganin

October 26, 2012

Abstract

In this project, a model is developed to describe the propagation of X-rays in a planar X-ray waveguide, based on an analytical solution to the inhomogeneous Helmholtz equation. This model is different to previous models as it takes absorption into account naturally through the complex index of refraction of the cladding material. A simple experiment is performed on a real X-ray waveguide to compare the model's results to; it is found that the model predicts many aspects of the behaviour of the real waveguide. One discovery that was of particular interest is the model's prediction of the Talbot effect inside a planar X-ray waveguide. It is believed that this model will prove useful in further work seeking to use X-ray waveguides to make lab X-ray sources behave more coherently; this will have applications, for example, in performing phase-contrast imaging with conventional X-ray tubes.

Contents

1 Introduction

1.1 Coherent and Incoherent Imaging

X-rays are an extremely useful illumination source for imaging a large range of different types of samples, from biological samples such as cells and proteins through to metallic structures. They have an advantage over visible light in that they penetrate many kinds of matter (particularly biological samples) much more effectively than visible light. Furthermore, biological samples show natural propagation-induced phase contrast with X-rays without the need for staining the sample with dyes, which is commonly required for light microscopy.

The simplest way of imaging a sample with X-rays is to illuminate it with an X-ray light field and place an imaging plate directly behind the sample. This is known as a contact image and is the scheme that is used in a medical chest X-ray, for example. However, the resolution attainable with this method is very low.

To perform high-resolution microscopy with X-rays, a coherent source, such as a synchrotron, is required, so that the photons striking the sample are all in-phase with each other. The sample is illuminated with this source, and a diffraction pattern is recorded with a detector in the far-field. What is recorded is the Fourier transform of the scattering potential of the sample – in practice, this scattering potential is the electron density [1]. However, the detector can capture the intensity, but not the phase, of the X-ray field – this phase has to be iteratively approximated using a computer algorithm. Once this is complete, the sample's projected electron density is known and it has been imaged successfully.

Another possible X-ray imaging technique is phase-contrast imaging. In the simplest implementation of this scheme, an X-ray wavefield strikes a weakly absorbing (usually biological) sample. This changes the shape of the wavefronts as different sections of the sample shift the phase of the incident radiation by a different amount. They are then allowed to propagate through some intermediate distance and hence the waves scattered from different parts of the sample interfere with each other. When the wavefront strikes the detector, a series of light and dark fringes are recorded representing the interfaces between different media in the sample [2]. This technique is demonstrated in figure 1.

1.2 Lab X-Ray Sources

Both of the high-resolution imaging techniques outlined in the previous section require that the incident radiation on the sample be spatially and temporally coherent. In practice, this means that the experiments can only be performed at a synchrotron, where intense radiation is produced from electrons as they are bent by magnetic fields. Because the radiation is so intense, it is feasible to filter it with a monochromater,
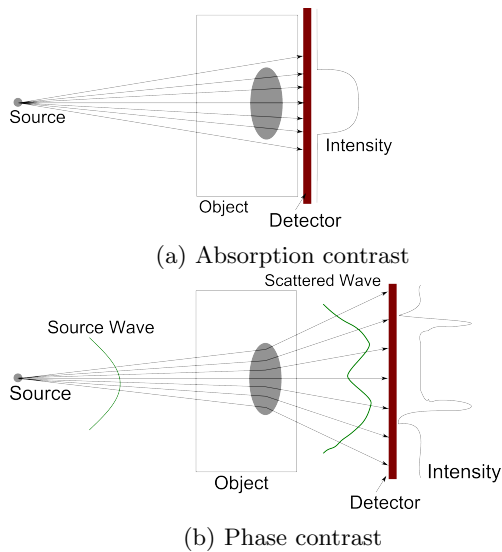

(a) Absorption contrast

(b) Phase contrast

Figure 1: Difference between a contact image (a) and a phase-contrast image (b). The propagation distance in (b) gives the scattered wave a chance to interfere with itself.
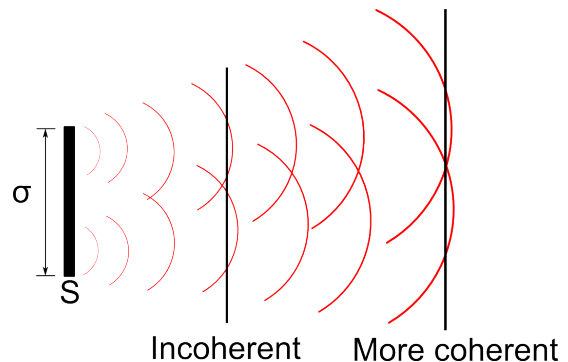

Figure 2: Incoherent source S with finite extent σ behaves coherently at large propagation distances

leading to temporal coherence, and because the effective source size is small, it is spatially coherent too. A synchrotron is an expensive piece of equipment however, and consequently beam time is hard to get for researchers. It would be ideal if the imaging tools described above could be used in an ordinary lab.

Unfortunately, conventional X-ray sources do not have the level of coherence required for this kind of imaging. In a lab X-ray tube, photons are generated by the collisions of an electron beam with a (usually) copper target. Incident electrons knock out inner-shell electrons from the copper atoms. The resultant holes are filled completely independently by other electrons in the atom relaxing, with no relation to what is happening in other atoms. Thus, the photons generated from these relaxations have absolutely no phase relationship to each other and are incoherent.

However, the situation is salvageable – there are ways to make an incoherent optical source appear to be more coherent, from the point of view of doing an imaging experiment.

One such way is for a slit to be placed in front of the source; then, far away from it, the source appears to be a point emitter and hence is coherent. This is illustrated in figure 2. However, one of the results of this technique is that the intensity of the source is much reduced; imaging experiments can take an infeasibly long time.

1.3 An X-Ray Waveguide

A better way for increasing the coherence of an X-ray tube is to use a waveguide. A waveguide is described in [3] as a structure which confines electromagnetic radiation within it as the radiation propagates through the waveguide. Perhaps the most common example of such is the glass optical fibre, which confines light within a guiding core of a higher refractive index than a cladding material.

This works because, as is explained in [3], visible light incident on an interface from the higher refractive index material can be totally internally reflected if the grazing angle is low enough. For X-rays, however, the situation is reversed – all matter has a complex refractive index for x-rays of $n = 1 - \delta + i\beta$, with the real part of n being less than one. This means that, in fact, if an X-ray is incident on a vacuum-matter boundary from the vacuum side, it will be totally *externally* reflected if the grazing angle is below an angle known as the critical angle.

A planar X-ray waveguide has the structure given in figure 3. If one considers a ray-optical picture, the waveguide operates by repeatedly bouncing low-angle rays between the two silicon slabs due to total external reflection; thus, the electromagnetic radiation is contained within the core and the incident wave is guided.

A waveguide is a useful tool for increasing the coherence of an x-ray tube because the gap between the two silicon pieces is so small; in this project, a waveguide with a slab gap of 500 nm has been studied. It is capable of accepting radiation which strikes it at any angle less than the critical angle (for silicon, this is 0.22° at 8 keV [4]), and the effective source size for the sample downstream of the waveguide is equal to the slab gap (i.e. very small!). The divergence of the field at the exit surface of the waveguide is also small. Such waveguides are discussed in detail in [5].

Such a waveguide might be used in an imaging experiment such as the one described in figure 4. Parabolic mirrors could be used to collimate the light, so that the divergence of the source is less than the critical angle of the waveguide – maximising the amount of light striking the waveguide that can be
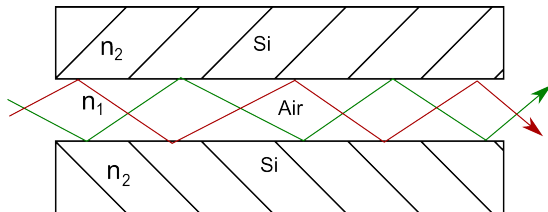
Figure 3: Schematic diagram of the construction of a planar x-ray waveguide. It guides light due to the total external reflection of low-angle rays striking the air-silicon interface.

Figure 4: An example of a phase-contrast imaging experiment that might be performed with a lab x-ray tube and a waveguide. An X-ray source S is focused by parabolic mirrors M, into a waveguide W. The exit of the waveguide is effectively a coherent source S', the radiation from which strikes a sample O. A detector D records a phase-contrast image of O.

accepted. The waveguide itself can then act as a spatially coherent source of radiation for a phase-contrast imaging setup.
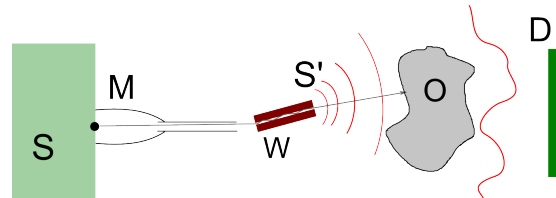
The method most often used to calculate the field inside the waveguide is to directly solve the parabolic wave equation numerically. For a planar waveguide, an analytical solution is possible, and models based on this solution have been published (see for example [5]). However, previous models did not take absorption into account naturally via the complex index of refraction; developing such a model is one of the principal objectives of this work.

1.4 Project Objectives

The purpose of this project was to characterise a particular X-ray waveguide. It is hoped that an understanding of the properties of this waveguide, from both a theoretical and experimental standpoint, will help enable coherent imaging experiments at Monash with conventional X-ray tubes in the near future.

The first, and principal, stage of this project was to produce a theoretical treatment of a planar waveguide that naturally accounts for absorption in the cladding material via the complex part of the index of refraction. Such a model has not been previously developed – absorption is usually artificially introduced via a so-called effective linear attenuation coefficient, denoted μ. Computer algorithms for solving the relevant equations were then developed, and subsequently written up as a computer program in the Python programming language.

The role of the computer model is to generate plots of various physical quantities of the wavefield inside the waveguide, for different kinds of waves striking the waveguide's entrance surface. The end goal was for the simulation to consider what the output from the waveguide is when it is illuminated with a radiation profile similar to a laboratory X-ray tube.

The final part of the project was to design and execute an experiment that measures the output radiation of the waveguide when it is illuminated with an X-ray source. The comparison between this measurement and the results of the simulation gives a measure of how well the model characterises the waveguide in question.

2 Background Theory

2.1 Coherence

Thus far, radiation has been referred to as coherent or incoherent in a fairly hand-wavy manner. In this section, the precise meaning of the term "coherent" will be explained.

Hecht [6] describes two different kinds of coherence – temporal coherence, and spatial coherence. Temporal coherence is about the bandwidth of the source (i.e. the range of wavelengths emitted from it); spatial coherence is about the spatial extent of the source (i.e. how big it is).

More specifically, a source with a high temporal coherence (i.e. a very small bandwidth) emits radiation within a very narrow wavelength range. This means that if the wavefronts of two plane waves emitted by this source are well synchronised with each other at one point in space, then they will remain relatively synchronised with each other as they propagate for a period of time known as the coherence time (or, alternately, for a distance known as the longitudinal coherence length).

If a source has a high degree of spatial coherence at some plane downfield of the source, then that means that the phase of the radiation at various points along this plane is highly correlated. The length over which there is a correlation on this plane is known as the spatial coherence length.

The spatial coherence of a source at a plane of interest depends on the effective size of the source at this plane. As was alluded to in the introduction, the effective extent of the source for the purposes of coherence can be reduced by placing it farther away from the experiment; it then appears to be more like a point-source and hence spatially coherent. This is what is shown in figure 2.

2.2 Waveguides

A waveguide is a structure that confines electromagnetic radiation within it as it propagates through. As was explained in the introductory material, this project has focused on the simplest type of waveguide – a quasi 2-dimensional planar waveguide, illustrated in figure 3.
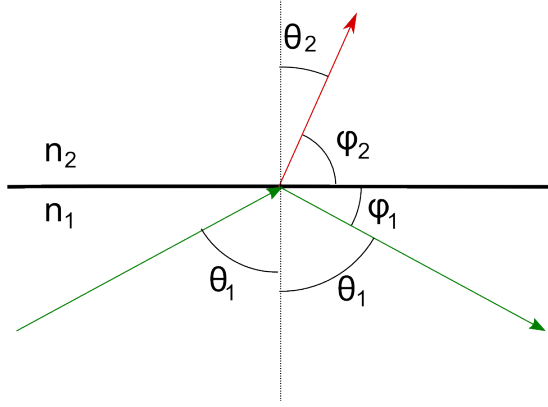
Figure 5: Snell's law defines the angle at which a light wave incident on a boundary between two media with refractive indices n_1 and n_2 will refract into the second media.
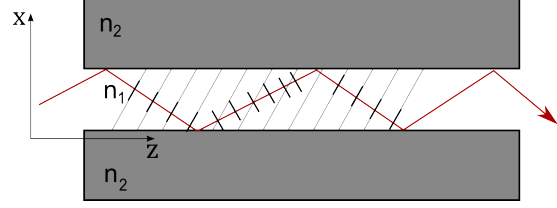

Figure 6: The self-consistency criterion for waveguide modes. The criterion is satisfied if the incidence angle is such that the twice-reflected wave matches up with the original wave.

2.2.1 Total External Reflection and the Critical Angle

In the introduction, the mechanism for the confinement of electromagnetic radiation between the two slabs of the planar waveguide was identified as total external reflection. This phenomenon can be understood in terms of Snell's law [6], in equation (1).

$$n_1 \sin \theta_1 = n_2 \sin \theta_2 \qquad (1)$$

When light is incident on an interface at an angle θ_1 relative to the normal between two media with refractive indices n_1 and n_2, in general, a component of the light is transmitted through the interface at an angle θ_2, and a component is reflected from the interface at an angle equal to the angle of incidence. This is illustrated graphically in figure 5.

In X-ray optics, however, light usually strikes the interface at a very small grazing angle (i.e. the light travels nearly parallel to the interface). Thus, it is convenient to replace the angles of incidence and reflection relative to the normal of the plane of incidence in equation (1) (θ_1 and θ_2) with angles relative to the plane of incidence (ϕ_1 and ϕ_2). This allows us to recast equation (1) into the form given in (2).

$$n_1 \cos \phi_1 = n_2 \cos \phi_2 \qquad (2)$$

Total external reflection occurs when given n_1, n_2 and ϕ_1, with $n_1 > n_2$, there are no real solutions for ϕ_2 in equation (2). This regime includes all angles of incidence above some critical angle for which $\phi_2 = 0$. If we have an air-matter interface, with the air having a refractive index of 1 and the matter having a refractive index of $n = 1 - \delta$ (neglecting the complex part in the present discussion), an expression for this critical angle can be derived. By substitution of these parameters into equation (2), one obtains

$$\cos \phi_1 = 1 - \delta$$

Applying the small-angle expansion for cosine yields an expression for the critical angle.

$$\phi_{\mathrm{crit}} = \sqrt{2\delta} \qquad (3)$$

When an X-ray wave is incident on the waveguide at a grazing angle higher than ϕ_{crit}, no part of the wave is transmitted through the interface (although, as will be subsequently discussed, this does not mean that all of the radiation is reflected either – there can be loss in this process).

2.2.2 Guided Modes

One characteristic of a waveguide is that arbitrary waves cannot propagate through them; only a discrete set of electromagnetic waves known as guided modes can travel through the waveguide.

This result is derived in [3] in terms of self-consistency and is illustrated in figure 6. The requirement is imposed that if a plane wave is reflected off the waveguide interface, and this reflected wave is again reflected off the other interface, the twice-reflected wave is a copy of the original plane wave. This

condition is nescessary in a waveguide because without it, the twice-reflected wave would interfere with the original wave, and over many reflections, the average intensity would be zero.

The self-consistency requirement is satisfied for a discrete set of incidence grazing angles of the plane wave on the waveguide interface; this set will be referred to as ϕ_m.

Before the self-consistency criterion illustrated in figure 6 can be used to geometrically derive a mathematical expression for the set of mode angles ϕ_m, what exactly occurs at the interface must be considered. In the simplest case, the waveguide cladding is a perfect X-ray mirror, and so the reflected radiation undergoes a phase shift of π on reflection. However, this is not the physical reality for the waveguide in this project; it is made of silicon, which behaves as a dielectric material optically.

There are two main consequences of the use of a dielectric material in place of an ideal mirror as the waveguide cladding material. Firstly, the phase shift on reflection is not π, but some other material-dependant number (it is in fact given by the Fresnel reflection coefficients in [3]). Secondly, the wavefunction of the incident light field does not abruptly stop at the interface; instead, a so-called evanescent wave penetrates a small distance into the cladding material.

If loss in the waveguide is neglected for the moment, an expression for the wavefunction of a guided mode can now be postulated using physical intuition. The self-consistency principle implies that, since a reflected wave farther along the waveguide optical axis must replicate the original incident wave, the shape of the wavefunction must be invariant to propagation along this direction. This in turn suggests that the shape of the wavefunction in the core must be a standing wave. In the cladding, we require that there is an exponentially-damped evanescent wave due to the imperfect "hardness" of the reflections from a dielectric material.

Fuhse [5] uses these ideas to postulate a wavefunction of the form given in equations (4), (5), and (6). In these expressions, and for the remainder of this report, x and z are the transverse and longitudinal coordinates respectively (as depicted in figure 6), λ is the wavelength of the source, $k = \frac{2\pi}{\lambda}$, and k_z and k_x are the x and z-components of the wavenumber k. The extent of the waveguide is from $-d$ to 0, where d is the gap between the two cladding slabs.

$$\psi_m (x, z) = \psi_m^x (x) \cdot e^{ik_z z} \tag{4}$$

$$\psi_m^x (x) = \begin{cases} B \cdot \exp(-\gamma x) & x \geq 0 \\ B \cdot \cos(k_x x) + C \cdot \sin(k_x x) & -d < x < 0 \\ (B \cdot \cos(k_x d) - C \cdot \sin(k_x d)) \exp(\gamma (x + d)) & x \leq -d \end{cases} \tag{5}$$

$$\gamma = \sqrt{k^2 - k_x^2 - n^2 k^2} \tag{6}$$

The veracity of this expression can be proved by showing it is a solution to the inhomogeneous Helmholtz equation (7). In this equation, k_0 is the free-space wavenumber, and $n k_0$ is the wavenumber in the media. The waveguide being studied in this project has an air gap as a core material, so it is assumed that the refractive index of the core is 1 and hence that all losses result from the cladding.

$$\nabla^2 \psi + n^2 k_0^2 \psi = 0 \tag{7}$$

This is discussed in [5], where equation (5) is confirmed as the expression for the wavefunction for the modes in an X-ray waveguide. For each mode, the angle of incidence is different, and hence the projection of k onto the x-axis k_x is different. This leads to different values of γ, B and C for each mode wavefunction.

2.2.3 Solution of Guided Modes

The wavefunction of an electromagnetic wave in the presence of dielectric-vacuum interfaces, such as the ones in the waveguide being studied here, must be smooth and continuous across the interface. With reference to equation (5), this implies that at $x = 0$, the first two parts of ψ_m^x and their derivatives are equal, and at $x = -d$, the latter two parts and their derivatives are equal.

These conditions lead to a set of simultaneous equations for B and C in terms of k_x. These equations are written out in matrix form in equation (8).

$$\begin{bmatrix} \gamma & k_x \\ k_x \tan(k_x d) - \gamma & \gamma \tan(k_x d) + k_x \end{bmatrix} \begin{bmatrix} B \\ C \end{bmatrix} = \begin{bmatrix} 0 \\ 0 \end{bmatrix} \tag{8}$$
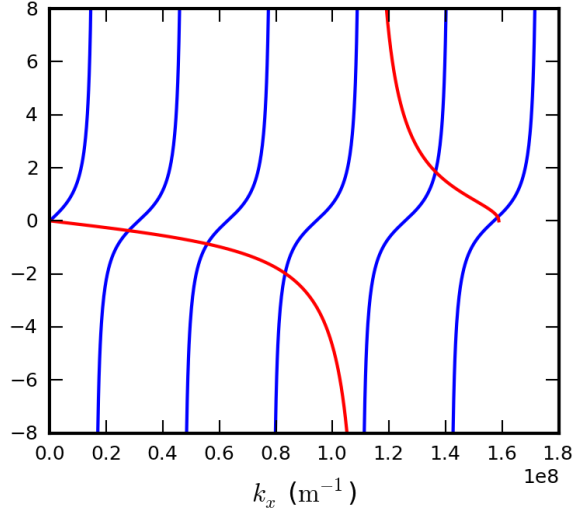
Figure 7: Graphical solution of the transcendental in equation (9) for k_x. The blue line is the left hand side of (9), and the red line the right. Each intersection corresponds to a solution and hence a mode. Note that, for simplicity, this plot is for a waveguide with a slab gap of 100 nm (and hence fewer guided modes)

This system of equations is homogeneous (i.e. the right-hand side is the zero vector). This means that it has non-trivial solutions for B and C only when the determinant of the matrix is zero. Setting this determinant to zero leads to the following equation.

$$\tan\left(k_x d\right) = \frac{2 k_x \gamma}{k_x^2 - \gamma^2} \tag{9}$$

This transcendental equation can be solved numerically or graphically for k_x; this is shown in figure 7. The plot in this figure ends when k_x becomes large enough that γ in equation (9) becomes imaginary. The number of solutions to this equation gives the number of guided modes that the waveguide supports.

The solutions to equation (9) can be substituted back into equation (8); this allows the solution of these simultaneous equations for B and C for each value of k_x. However, since the matrix in equation (8) is singular, there is a free variable in the solutions (i.e. there is a relationship between B and C, but no absolute solution for them). This makes physical sense; the absolute amplitude of the wavefunction will depend on the intensity of the radiation illuminating it; the role of the constants B and C are to make sure that the core wavefunction joins smoothly with the cladding wavefunction. Computationally, it is sufficient to set one of the values to one, which gives a well-defined value for the other. In this way, a complete expression for each of the guided modes in the form of equation (5) can be found.

2.2.4 Radiative Modes

It will prove useful shortly to consider what happens to radiation which strikes the waveguide at an angle *greater* than the critical angle in equation (3). As is depicted in figure 2, a portion of the radiation will be transmitted through the interface, and a portion will be reflected. Since, on each "bounce" of the wave on the cladding, a portion of the energy is transmitted out of the waveguide, the intensity of the field inside the waveguide quickly drops to zero as it propagates.

The mathematical form of this kind of wave would be very different to that in equation (5) for a guided mode. In the cladding, since a part of the wave has been refracted into it, the form is no longer a damped evanescent wave, but rather something that propagates and carries energy (for example, a plane wave). In the core, the intensity needs to be exponentially damped as a function of z. A more precise mathematical form of the guided modes is, however, not nescessary for this project.
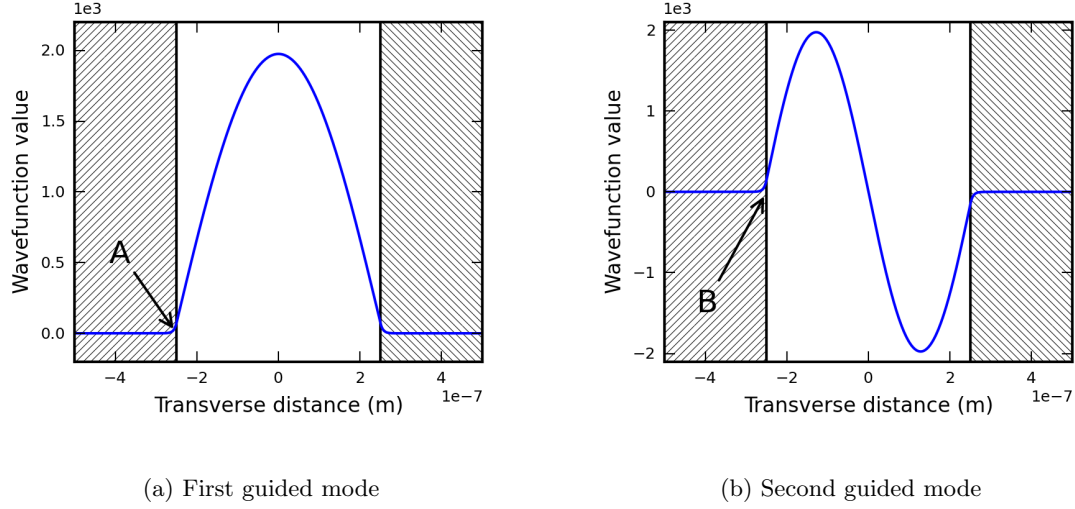
(a) First guided mode

(b) Second guided mode

Figure 8: The real part of the wavefunction under lossless conditions for the (a) first and (b) second guided mode. The shaded parts represent the waveguide cladding; the wavefunction penetrates the cladding at points A and B.

2.2.5 Coupling

It follows from the self-consistency principle that any wave in the waveguide that is not in the form of a guided mode will rapidly dampen out to zero, due to destructive interference with itself. Thus, sufficiently far into the waveguide, the field consists solely of a superposition of guided modes [5]. If each mode $\psi_m(x,z)$ is weighted by a coefficient c_m, then the wavefunction in the waveguide is given by equation (10).

$$\psi(x,z) = \sum^{m} c_m \psi_m(x,z) \tag{10}$$

In terms of linear algebra, the guided and radiative modes together form a basis for all possible waves using such a superposition. However, the guided modes alone do not; thus, especially close to the critical angle, a wave incident on the waveguide need not couple all of its intensity into the waveguide (this is to say, $\sum |c_m|^2 < 1$).

The next question that arises is, how is the set of coefficients c_m calculated? Continuing the line of thinking based on linear algebra, the coefficient for a particular mode wavefunction is the projection of the incident field onto this wavefunction. This is given in [5] as the following overlap integral.

$$c_m = \int_{-\infty}^{\infty} \psi_{in}^*(x, z=0)\, \psi_m(x, z=0)\ \mathrm{d}x \tag{11}$$

2.2.6 Loss

Thus far, the waveguide cladding material has been considered to be perfectly lossless. However, a key part of this project is the treatment of attenuation of the wave inside the waveguide due to absorption of the radiation. In this section, an overview will be given of how loss has previously been accounted for.

As is evident from equation (5), some part of the wave exists inside the waveguide, and some (small) part of it exists in the cladding. This is graphically illustrated in the plot of the first and second guided modes in figure 8.

If the cladding is a real material with a complex index of refraction $n = 1 - \delta + \beta i$, then the imaginary part of the refractive index describes the extent to which the material absorbs X-rays. The refractive index is, of course, wavelength-dependant (this fact will be encountered during the modelling later on in this report). Some part of the radiation that exists in the cladding can now be absorbed by the material. This reduces the amplitude of the wavefunction in this region; of course, to maintain the continuity of the wavefunction, the intensity in the core also has to be lowered to match. The physical description for what is happening in this process is that energy flows out from the center of the waveguide into the

cladding, where it is absorbed. The amplitude of the wavefunction decreases as it propagates in z as a result of this loss.

In previous work, such as [5] and [7], this has been taken into account by including an effective linear attenuation coefficient μ_m in equation (4). This coefficient bundles up information about both how much of the wavefunction exists in the cladding, and how readily this is absorbed. As a result, the expression for the waveguide modes is now as in equation (12); $\psi_x(x)$ has the same value as previously in equation (5).

$$\psi_m(x,z) = \psi_m^x(x) \cdot e^{ik_z z} \cdot e^{-\mu_m z} \tag{12}$$

This approach has some disadvantages. Firstly, because every mode has different amounts of its wavefunction sitting in the cladding material, the value of μ_m is different for each mode; this value must be looked up somewhere or calculated in order to describe the waveguide adequately.

Secondly, although this equation describes the attenuation of the wavefunction in the z-direction, it does not offer any insight into the energy flow into the cladding that was mentioned above. Even with the inclusion of the attenuation coefficient, the form of the wavefunction in the x-direction is still a standing wave, which does not allow for any energy flow in this direction. Thus, in the presence of loss, equation (12) can only be an approximation to the true wavefunction.

In this project, a different approach will be followed. The loss of the wavefunction will be seen to arise naturally from the complex index of refraction by considering complex solutions to equation (9) and pushing the analysis through with a complex value of k_x.

3   Modelling

The main body of work in this project has been the development of a computer model to describe the behaviour of a planar waveguide with air in the core. The backbone of this model is a treatment whereby the loss arises naturally from the complex index of refraction of the cladding material. This model is then interrogated to look at the waveguide's behaviour when illuminated with radiation of varying degrees of coherence. A wide range of physical quantities are analysed, including the intensity, phase, Poynting vector, and both real and imaginary parts of the wavefunction.

3.1   Model Development

3.1.1   Wavefunction Form

The starting point for the model is the mode wavefunction expression in equations (4) to (6). However, for convenience, a different but equivalent form will be used instead. The standing wave represented by a sum of a sine and a cosine in equation (5) will be replaced by a sum of two unbalanced, counter-propagating plane waves. Although the model would work equally well using equation (5) as a wavefunction form (given complex values for B and C), the counter-propagating plane-waves make it more obvious that the wavefunction is *not* a standing wave when n is complex.

The counter-propagating plane-waves paint a helpful physical picture of the wavefunction being continuously reflected by the cladding material, as is the case in figure 6. In general, they will be allowed to be unbalanced by some functions of x $B(x)$ and $C(x)$. For convenience, the coordinate system will also be shifted, so that in the x-direction, the waveguide is centered on $x=0$ and extends from $x=-\frac{d}{2}$ to $x=\frac{d}{2}$. Thus, the x-component of the wavefunction can be written in the following form.

$$\psi_m^x(x) = \begin{cases} Ae^{-\gamma\left(x-\frac{d}{2}\right)} & x \geq \frac{d}{2} \\ B(x)e^{ik_x x} + C(x)e^{-ik_x x} & -\frac{d}{2} < x < \frac{d}{2} \\ De^{\gamma\left(x+\frac{d}{2}\right)} & x \leq -\frac{d}{2} \end{cases} \tag{13}$$

It turns out that the only possible forms of $B(x)$ and $C(x)$ that satisfy the Helmholtz equation (7) are constant functions, or other functions that are equivalent to constant functions in the context of equation (13) (such as e^x, which can be absorbed into the exponent already in equation (13)). Thus, the model being developed in this project will utilise eigenmodes of the form in equation (14).

$$\psi_m^x (x) = \begin{cases} Ae^{-\gamma\left(x-\frac{d}{2}\right)} & x \geq \frac{d}{2} \\ Be^{ik_x x} + Ce^{-ik_x x} & -\frac{d}{2} < x < \frac{d}{2} \\ De^{\gamma\left(x+\frac{d}{2}\right)} & x \leq -\frac{d}{2} \end{cases} \tag{14}$$

If the conditions that the wavefunction must be smooth and continuous are now applied as previously, an equation analogous to equation (8) can be obtained. This is presented in equation (15). Setting the determinant of this system equal to zero yields a transcendental equation (16) which is analogous to equation (9) and can be used to solve for the value of k_x for each mode.

$$\begin{bmatrix} -1 & e^{ik_x\frac{d}{2}} & e^{-ik_x\frac{d}{2}} & 0 \\ 0 & e^{-ik_x\frac{d}{2}} & e^{ik_x\frac{d}{2}} & -1 \\ \gamma & ik_x e^{ik_x\frac{d}{2}} & -ik_x e^{-ik_x\frac{d}{2}} & 0 \\ 0 & ik_x e^{-ik_x\frac{d}{2}} & -ik_x e^{ik_x\frac{d}{2}} & -\gamma \end{bmatrix} \begin{bmatrix} A \\ B \\ C \\ D \end{bmatrix} = \begin{bmatrix} 0 \\ 0 \\ 0 \\ 0 \end{bmatrix} \tag{15}$$

$$\det\left(\begin{bmatrix} -1 & e^{ik_x\frac{d}{2}} & e^{-ik_x\frac{d}{2}} & 0 \\ 0 & e^{-ik_x\frac{d}{2}} & e^{ik_x\frac{d}{2}} & -1 \\ \gamma & ik_x e^{ik_x\frac{d}{2}} & -ik_x e^{-ik_x\frac{d}{2}} & 0 \\ 0 & ik_x e^{-ik_x\frac{d}{2}} & -ik_x e^{ik_x\frac{d}{2}} & -\gamma \end{bmatrix} \right) = 0 \tag{16}$$

3.1.2 Considering a Complex Index of Refraction

As was previously discussed in the introduction and theory sections, real materials which absorb some fraction of the X-rays striking them have a complex index of refraction $n = 1 - \delta + \beta i$, with the imaginary part encapsulating information about this loss. In this section, the effect of a complex refractive index on equation (14) will now be considered.

If n is allowed to be complex, then the value for γ in equation (6) is complex in general. This makes the solution to k_x in equation (16) complex too. If k_x is complex, then since $k = \frac{2\pi}{\lambda}$ and $k^2 = k_x^2 + k_z^2$, this makes k_z complex. A complex k_z allows equation (4) to be rewritten as in equation (17).

$$\psi_m (x, z) = \psi_m^x (x) \cdot e^{i\text{Re}(k_z)z} e^{-\text{Im}(k_z)z} \tag{17}$$

This equation now includes an exponential decay term in the longitudinal z coordinate (in fact, $\text{Im}(k_z)$ is equivalent to the linear attenuation coefficient μ_m in equation (12)). It is reasonable to expect, therefore, that the consideration of complex n will lead to loss in the waveguide, as physically happens. Additionally, since k_x will be complex, the form of the middle part of equation (14) will not be a standing wave, but rather include some energy flow. The direction of this energy flow is, however, not immediately obvious; it will be later analysed with the results of the computational implementation of the model.

To continue the development of the model, the complex expression for γ must be substituted into equation (16) to get a set of solutions for k_x of each guided mode in the waveguide. These solutions must then be inserted into equation (15) to obtain the coefficients A, B, C and D and hence obtain a complete expression for the wavefunction of this guided mode according to equation (14).

3.1.3 Projection onto Eigenmodes

So far, the model is capable of explaining the propagation of individual eigenmodes through the waveguide. The next step is to consider what happens when a plane wave with some arbitrary incidence angle strikes the waveguide. Obviously, some superposition of guided modes will be excited in the waveguide, and the weightings for this superposition can be determined by the overlap integral in equation (11) as described in the introduction.

3.1.4 Incoherent Superposition of Plane Waves

The previous section describes the waveguide's behaviour in a monochromatic, and therefore perfectly coherent, field. However, as discussed in the introduction, an X-ray tube produces radiation that is relatively incoherent and contains a spread of wavelengths. However, any field can be expressed by a sum of plane waves (using Fourier decomposition). Thus, a stochastic picture can be adopted, whereby the
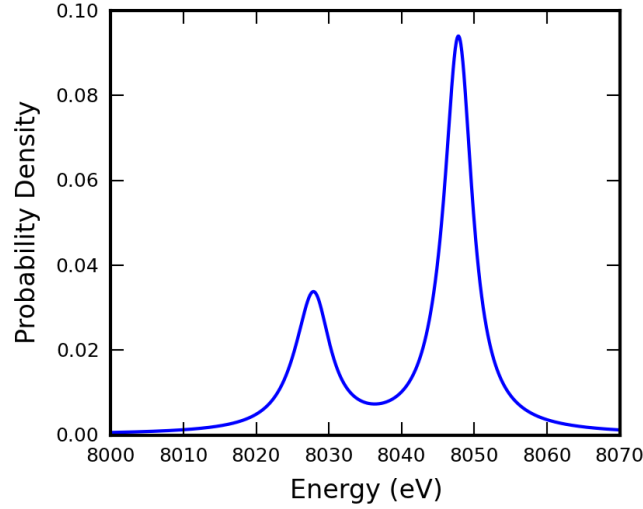
Figure 9: The probability density function for the emission energy of X-rays from a copper target. The form is a sum of four Lorentzians from [8].

waveguide is illuminated by a sequence of plane waves with an angle and a wavelength randomly chosen from a distribution.

In this project, the angular distribution will be considered to be normal, with a center corresponding to the geometric incidence angle of the X-ray source on the waveguide, and a width that gives a measure of how incoherent the source is. The wider the angular distribution striking the waveguide, the less coherent the radiation there is. Different values of this width will be experimented with in this project to simulate different conditions.

The wavelength spread of the source, however, should be largely invariant under changes to the experimental conditions. Almost all of the intensity of the source is in the K_{a1} and K_{a2} emission lines. The distribution of intensity between these two emission lines, and the width of the lines, is a fundamental property of the target material (copper) and not related to the rest of the source (so long as the electron energy is high enough to knock out the inner-shell electrons). In [8], an expression for the intensity of the emitted radiation as a function of energy is given in terms of four Lorentzians; this distribution is shown in figure 9.

Each one of the generated plane waves can be coupled into the waveguide via equation (11); the question arises, what is the observable intensity at a screen placed downstream of the waveguide? There are many incident plane waves, and via the overlap integral, each one of these plane waves has a weighted sum of mode eigenfunctions associated with it. When answering this question, it is important to consider which wavefunctions are able to interfere with each other.

For an individual plane wave coupling into the waveguide, the guided mode wavefunctions it excites will be able to interfere with each other, because they are driven from the same, coherent source. However, the guided mode wavefunctions excited from two different incident plane waves will not have any phase relationships with each other, because the incident waves they are generated from are uncorrelated. So, the mode wavefunctions from each individual incident wave should be added coherently (i.e. their *values* should be added), and then this quantity for each incident wave should be added incoherently (i.e. their *intensities* should be added).

This is succinctly expressed in equation (18), where ψ_{mn} is the eigenfunction in the nth mode excited by the mth incident plane wave, and z_0 is the exit surface of the waveguide.. Recall that the wavefunction in the far-field of the waveguide will be the Fourier transform $\mathcal{F}$ of the wavefunction at the exit surface of the waveguide [6].

$$I_{\text{Screen}} = \sum^{m} \left| \mathcal{F} \left(\sum^{n} \psi_{mn} \left(x, z = z_0 \right) \right) \right|^2 \tag{18}$$

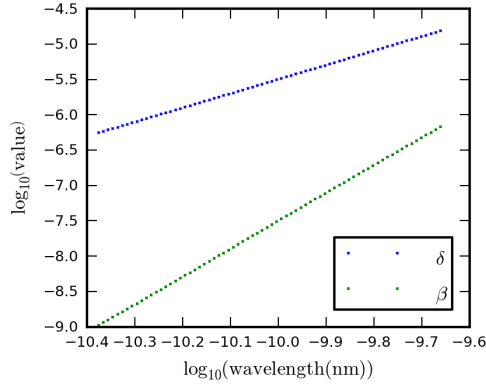This expression allows the simulation of an experimentally observable quantity – what the intensity

Figure 10: The real and imaginary part of the refractive index of silicon as a functon of wavelength. It is linear on log-log axes in the region of interest of this project.
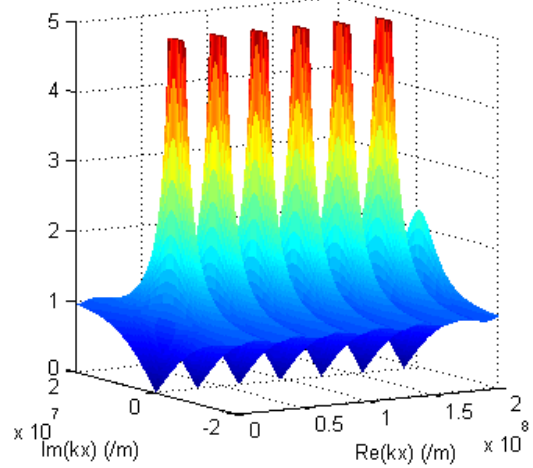

Figure 11: The magnitude of equation (9) as a function of the real and imaginary parts of k_x. The solutions correspond to the minima.

at a screen downfield of the waveguide looks like when the waveguide is illuminated by a collection of plane waves approximating a real X-ray source.

3.2 Model Implementation

The ideas presented in the previous section were encoded using the Python programming language, to produce a computer implementation of this model. Numerical routines from the NumPy and SciPy libraries [9] were used, and plots were generated with the Matplotlib library [10].

Numerical root-finding methods were used to solve equation (16) to obtain k_x for each waveguide mode. This value was then substituted into equation (15), whose null space was computed with a singular value decomposition, yielding a set of coefficients A to D for each waveguide mode.

To compute the intensity profile in the waveguide when it is illuminated by an arbitrary incident plane wave with angle θ, the overlap integral in equation (11) was evaluated numerically. Equation (10) was then used to obtain a total wavefunction that could be used to describe the intensity in the waveguide.

To evaluate the intensity profile in the waveguide when it is illuminated by incoherent radiation, the angular and wavelength distributions described in section 3.1.4 were used to generate random plane waves. The waveguide intensity profile was calculated for each of these plane waves, and these profiles were summed to get the result of incoherent illumination.

Most of the implementation is fairly straightforward; in this section, some of the interesting details will be discussed.

3.2.1 Describing the Waveguide

Earlier on, it was mentioned that in general, the refractive index of a material changes as a function of wavelength. As described in a previous section, part of this model involves illuminating the waveguide with light consisting of a distribution of wavelengths – obviously, an accurate treatment will therefore require this change in n to be taken into account.

For a wide range of materials, the data for the X-ray refractive index as a function of energy is available from [4]. For silicon (which is the material of the waveguide that is studied in this project) and over a wavelength range of interest, the real and imaginary parts of the refractive index are plotted in figure 10. Away from any absorption edges, the data is linear on log-log axes. For the implementation of the model, a linear function was fit to these data sets and used to interpolate the value of n for any particular wavelength.

Absorption edges would introduce sharp discontinuities in this data. The data can still be used for interpolation by using a different line on either side of the edge, but this did not need to be implemented for this project.

3.2.2 Solving the Complex Transcendental

A large part of the work in this project was dedicated to finding a reliable numerical method for solving the transcendental determinant in equation (16). Whilst this may initially appear trivial, reliably finding a good approximation to the roots of this equation in the complex plane was deceptively difficult. The best algorithm that was discovered was a three step solution employing a variety of numerical methods.

The first step in this algorithm is to ignore the imaginary part of n, and to focus on finding all of the resulting real solutions to equation (9) (which is in fact equivalent to equation (16) and conceptually easier to think about). Looking at figure 7, it can be seen that the blue function (the left-hand side of equation (9)) is increasing for all k_x, and the red function (the right-hand side) is decreasing for all k_x. The blue function is periodically undefined with a period of $\frac{\pi}{d}$, and the red part is undefined at one point on the plot (where the sign of the denominator of the RHS of equation (9) changes). Furthermore, the red function stops when k_x becomes large enough to make γ imaginary.

The x-axis of this plot is then broken up into windows where the boundaries are the points at which either function is undefined. Since one side is always increasing, and the other always decreasing, within these windows of well-defined behaviour there will always be either zero or one intersection between the two lines. If the sign of the blue curve minus the red curve is different at either end of the window, there is a solution; else, there is no solution in the window. This means that a bracketing root-finding algorithm can be used; the `optimize.brentq` method from SciPy (which implements Brent's method [11]) was employed for this purpose.

After k_x has been found in the lossless case for all of the guided modes, the second stage of the algorithm commences. In this stage, equation (9) is considered as a vector function of two variables – it accepts $\mathrm{Re}(k_x)$ and $\mathrm{Im}(k_x)$ as parameters, and returns a 2-vector containing the real and imaginary part of the LHS - RHS of the equation. A plot of the magnitude of this function is shown in figure 11. The objective of this second stage is to find the roots of the depicted function by finding k_x that makes both components of this function zero, using all of the real k_x values obtained in the first stage as initial guesses to find all of the roots of this vector function.

The SciPy implementation of the Levenberg-Marquardt method [12] (in `optimize.root`) was used to find this root numerically. This method was chosen because although it is slower than other options, it is usually guaranteed to converge to a minima if one exists.

Unfortunately, the values of k_x found from this root-finding method were not accurate enough to make the matrix in equation (15) singular. A third stage of optimization was therefore added to the algorithm. The condition number of this matrix (defined as the ratio of the largest to the smallest singular value) was considered a scalar function of the real and imaginary parts of k_x, and the value of this function was numerically maximised. For this purpose, SciPy's `optimize.minimize` was used, with the Nelder-Mead method [13]. The value of k_x from the previous stage of the calculation was again used as the initial guess. It was found that the resulting values of k_x satisfied equation (16) sufficiently well.

Once k_x had been found for each guided mode, each value was successively substituted into equation (15). NumPy's `linalg.svd` method was then used to compute the singular value decomposition of this matrix. The right singular vector corresponding to the lowest (effectively zero) singular value was taken as the null space of equation (15), which is one of the infinitely many solutions to the equation. Thus, values for the coefficients A, B, C and D were found and hence the eigenfunction for every guided mode could be completely characterised.

3.2.3 The Poynting Vector

The Poynting vector is a quantity which gives the magnitude and direction of the energy flow of an electromagnetic wave. It is related to the gradient of the phase of the wave; in the case of a 1-dimensional wave as exists for energy flow in the transverse direction of a 2-d planar waveguide, it can be expressed as in equation (20). Note that a multiplicative factor in this equation has been ignored for simplicity.

$$\psi(x) = \sqrt{I(x)} e^{i\phi(x)} \tag{19}$$

$$S = I(x) \nabla \phi(x) \tag{20}$$

A naive computation of the Poynting vector could involve evaluating the phase of the wavefunction at all points on the x-axis by considering the angle of the complex value of the wavefunction on the Argand plane. Then, a numerical derivative of this function could be evaluated. However, this implementation is problematic because phase is only defined modulo 2π; there will be discontinuities in the phase where it

13

goes from π to $-\pi$, even though this has no physical meaning. Although these edges could be detected and removed, the algorithm is still relatively unstable because small bumps remaining at the edge could still put large spikes in the value of the derivative.

A more robust calculation for the Poynting vector can be performed by considering that the derivative of equation (19) can be written as in equation (21).

$$\psi'(x) = \frac{d}{dx}\left(\sqrt{I(x)}e^{i\phi(x)}\right) \tag{21}$$

By applying the product rule to equation (21), left multiplying by ψ^* and solving for $\phi'(x)$, one arrives at equation (22).

$$\phi'(x) = \frac{\mathrm{Im}\left(\psi^*(x)\psi'(x)\right)}{I(x)} \tag{22}$$

This equation gives the value of $\phi'(x)$, which is discontinuous and numerically difficult to calculate, in terms of $\psi'(x)$, which is smooth and continuous and therefore differentiable (this smoothness is enforced by equation (15)). This allows the expression of the Poynting vector S in equation (20) to be re-expressed as equation (23).

$$S(x) = \mathrm{Im}\left(\psi^*(x)\psi'(x)\right) \tag{23}$$

This expression can now be calculated with no explicit evaluation of the phase at all, and hence does not have the modulo 2π problems associated with the naive method. This is the method used in this model.

3.3   Simulation Results

In this section, various results from the execution of the model simulation are presented. Firstly, calculations for single eigenmodes are shown, to demonstrate that the correct behaviour is displayed. Then, calculations coupling single plane waves into the waveguide are shown, followed by calculations on incoherent superpositions of plane waves.

3.3.1   Single Mode Calculations

Figure 12 displays the real and imaginary parts of two of the guided mode wavefunctions produced by the model. Figure 13 is the Poynting vector of the second guided mode in the transverse x-direction, and figure 14 shows the intensity of the second guided mode at various propagation distances in the longitudinal direction. From these plots, some correct physical behaviour is visible.

As was enforced by the conditions in equation (15), both the real and imaginary parts of the guided mode wavefunctions are smooth and continuous. This gives confidence that the algorithm used for computing k_x and the null space of equation (15) is operating correctly.

The plot of the Poynting vector for the second guided mode in figure 13 displays the behaviour expected of it. The Poynting vector is positive for energy flow to the right, and negative to the left. It is seen therefore that energy flows out of the waveguide core and into the cladding, where it is lost. This flow is greater closer to the cladding, and zero at the very center of the waveguide. This behaviour could not be predicted using a linear attenuation coefficient model of the waveguide.

Figure 14 shows the intensity profile of the second mode at various propagation distances. In this plot, the intensity is seen to drop as the wave propagates; this is an observation of energy loss as predicted due to the complex value of k_z. The shape of the intensity profile, however, remains the same.

3.3.2   Plane Wave Illumination Calculations

Once it was verified that the single mode calculations behaved as expected, the simulation of plane wave coupling was then executed. The simulation coupled tilted plane waves of various angles into the waveguide by using the technique previously described to generate a wavefunction valid inside the waveguide. The square modulus of this wavefunction (the intensity) is plotted across the waveguide in both directions in figure 15.

The intensity profile when the waveguide is illuminated at normal incidence is shown in figure 15a. Unlike the other incidence angles in figure 15, this intensity map is symmetrical about the waveguide axis – matching the physical symmetry of the system being modelled. There are also two other features of this plot worth discussing.
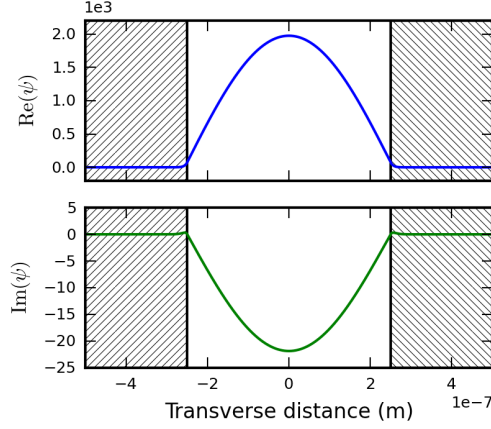
(a) First guided mode
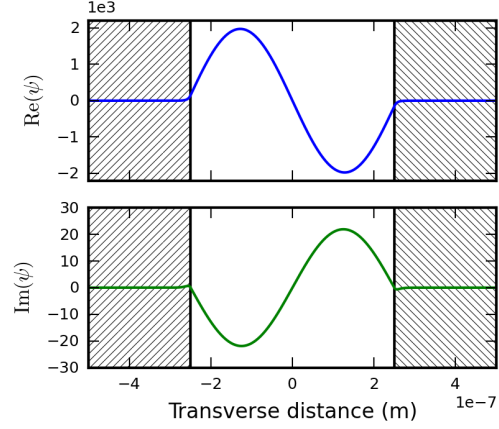
(b) Second guided mode

Figure 12: Wavefunctions for the (a) 1st and (b) 2nd guided modes of the wavefunction. Both the real and imaginary parts are smooth and continuous.
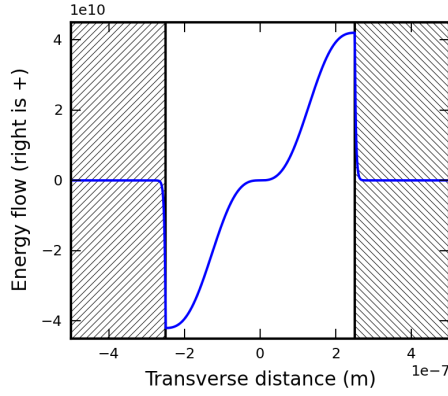

Figure 13: Poynting vector of the 2nd waveguide mode across the transverse profile. Energy is seen to flow into the cladding.
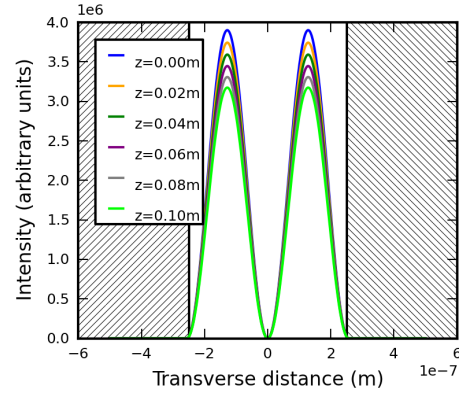
Figure 14: Intensity profile of the second guided mode at various propagation distances. Due to absorption effects in the cladding, the intensity drops as the mode propagates.

Firstly, the far left of the profile is a checkerboard pattern that looks a lot like diffraction off a slit. This is interesting, as this behaviour was not explicitly encoded into the model; it appears to be a natural consequence of equation (11).

Secondly, the diffraction pattern repeats itself periodically after some distance. This appears to be a manifestation of the Talbot effect, whereby a light field incident on a grating periodically produces images of this grating. The Talbot effect can be understood in terms of ray optics by considering the waveguide as a grating with a period of $2d$ (where d is the gap between the slabs) [14]. According to this geometric argument (displayed in figure 16), the so-called "revivals" present in figure 15a should occur with a period given by equation (24).
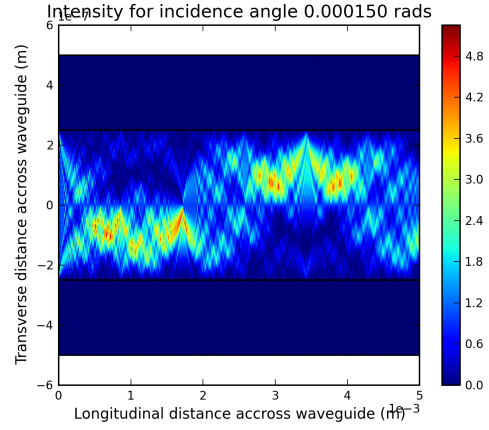
$$L = \frac{4d^2}{\lambda} \tag{24}$$

This does not, however, take into account the phase shift when a wave reflects off the waveguide slabs. If this is assumed to be π, as for a perfect mirror, than the revivals will occur with a period given by equation (25) [15].
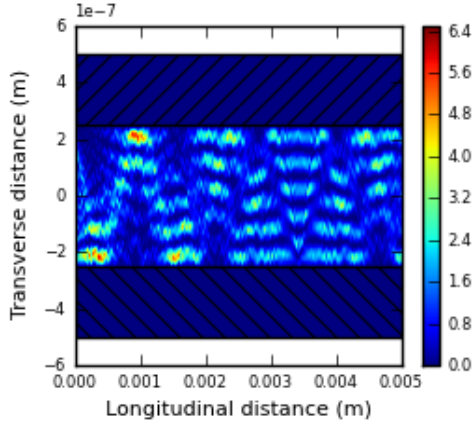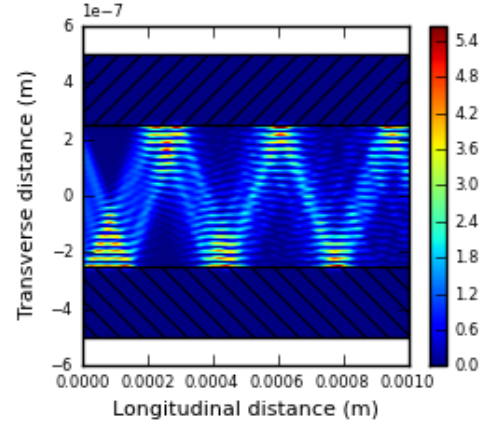
$$L = \frac{d^2}{\lambda} \tag{25}$$

15
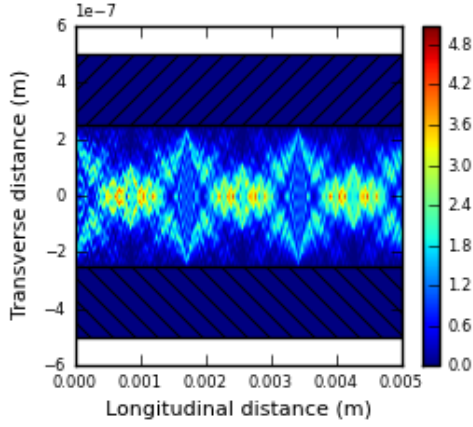
(a) Incidence angle = 0 radians

(b) Incidence angle = 0.00015 radians

(c) Incidence angle = 0.0008 radians

(d) Incidence angle = 0.003 radians

Figure 15: Intensity profile inside the waveguide when a plane wave incident at (a) 0 rads (b) 0.00015 rads (c) 0.0008 rads (d) 0.003 rads is coupled into the waveguide. Note that the horizontal axis in (d) has a different scale to the other figures.
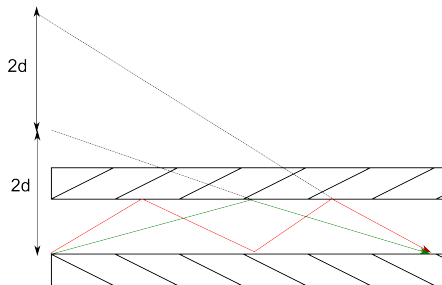

Figure 16: The geometrical argument behind light revival in a waveguide. The "grating" can be considered to be the virtual source of ray reflections off the waveguide cladding with a period $2d$. The revival occurs when the light rays from the two modes come together again.
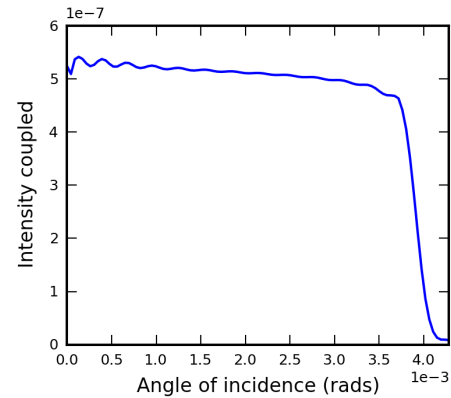

Figure 17: The amount of the incident wave coupled into the waveguide, as a function of plane wave incidence angle. There is a dramatic drop at the critical angle.

16

Name	Angular Distribution	Wavelength Distribution
Narrow	Normal; $\sigma = \frac{0.0033}{6}$ rads	Single wavelength
Wide	Normal; $\sigma = \frac{0.0033}{3}$ rads	Single wavelength
Polychromatic	Single angle	As in figure 9
Real	Normal; $\sigma = \frac{0.0033}{3}$ rads	As in figure 9

Table 1: Simulated X-ray sources used in this model. The angular distribution represents the spatial coherence, and the wavelength distribution the temporal coherence

This equation predicts a Talbot distance of 1.6 mm; the revivals in figure 15a appear to be at every 1.7 mm. The difference can be mostly explained by noting that the phase shift on reflection of a dielectric is not, in fact, exactly π.

Figures 15b to 15d display the coupled intensity for plane waves incident on the waveguide at various angles. In the highest angle wave (figure 15d, 0.003 radians), the ray optical nature of light is clearly evident. The "bouncing" beam of light in the cavity is propagating at an angle equal to the incidence angle, leading to the diagonal pattern evident in this figure.

This is not, however, the full story – when the beam comes close to the cavity walls, there are clear interference fringes visible. These fringes are almost identical to the fringes of a quantum-mechanical beam in a square potential, shown in [16]. They are in fact caused by the coherent interference between the incident beam striking the wall, and the reflected beam coming off it. The remaining angles between the two extremes gradually move between the bouncing interference present in figure 15d, and the Talbot pattern in figure 15a.

Another result of the coupling simulation that should be considered is how the efficiency of the coupling changes with incidence angle. Figure 17 shows a plot of the sum of the coupling coefficient amplitudes (i.e. $\sum |c_m|^2$) as a function of the incidence angle of a plane wave. It is seen that the amount of wave coupled gradually and slowly decreases for angles above normal incidence, until a very sharp drop around the critical angle. This is in line with what would physically be expected; for very high grazing angles, the projection of the wave onto the guided modes will be low – they will be projected mostly onto the radiative modes.

### 3.3.3 Incoherent Superposition Calculations

The next stage of the model was to simulate the waveguide when it is illuminated by both temporally and spatially incoherent light, such as that obtained from a lab X-ray source. Four "sources" were considered; their properties are tabulated in table 1. Each source used a probability distribution for the angle and wavelength of the plane waves it generated.

The response of the waveguide was simulated for each of the four sources at an incidence angle of 0, 0.00015, 0.0008, and 0.003 radians. For each source, a map of intensity in the waveguide (similar to figure 15) was generated, as well as the expected intensity at the far-field (using equation (18)). These results for selected combinations of interest are displayed in figures 18 and 19.

Figures 18a, 18c, and 18d show the fractal Talbot effect described in [14]. For the maps at normal and 0.00015 radian incidence angles, a revival of the original waveguide entrance field is visible at about 3.4 mm into the waveguide. Half way between the entrance and its image, two images of the entrance are seen on top of one another. One third of the way, there are three images present – the pattern continues, limited only by the resolution of the simulation.

The revival distance for these incidence angles appears to be double that predicted by equation (25) and shown in figure 15a. This is the same revival distance, however, that is shown in figure 15b for a coherent plane wave incident at a low grazing angle. The implication therefore is that equation (25) is only valid for radiation incident normally on the waveguide (which is in fact discussed in [14]), and when there is radiation incident at an angle, the true revival period is twice this.

In contrast, the high-grazing angle intensity plots (figures 18e and 18f) do not display a marked Talbot effect. There is perhaps a modulation of intensity in the transverse direction at the half-Talbot distance, but certainly nothing like the fractal patterns evident in the other images in figure 18. Instead, ray optical patterns are more evident – at the begining of both figures, a bouncing ray similar to figure 15b can be seen, losing intensity and coherence as it smears out into the rest of the waveguide.
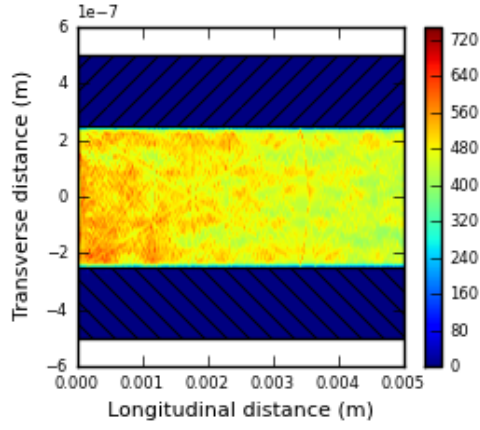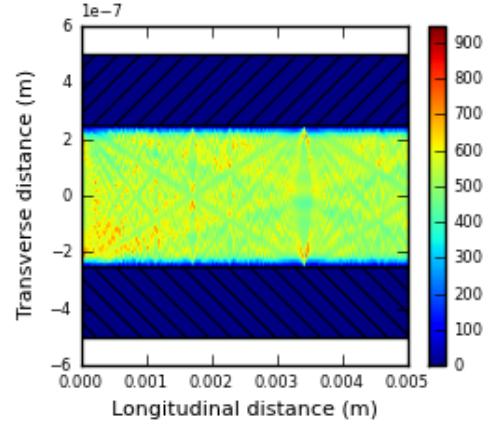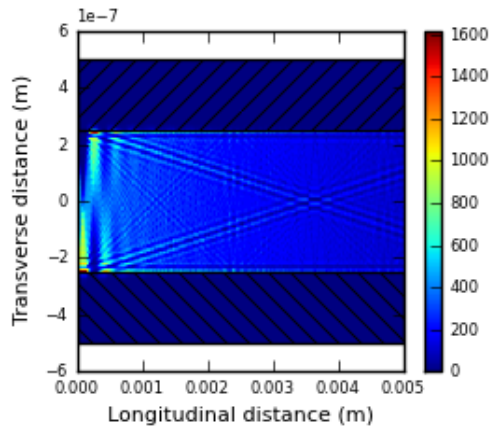
(a) Normal incidence, wide source
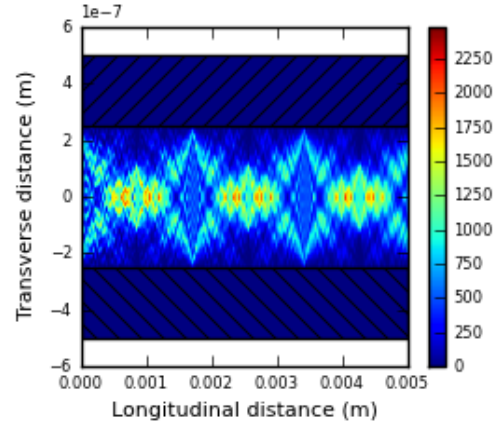
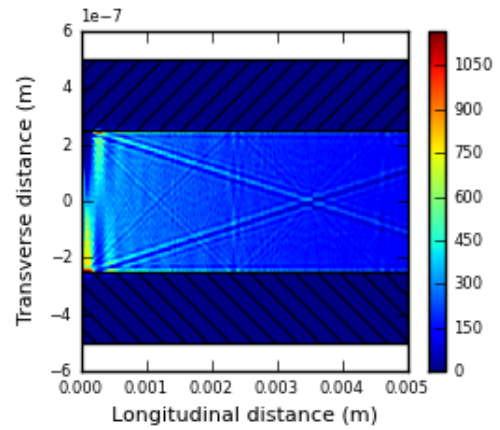(b) Normal incidence, polychromatic source
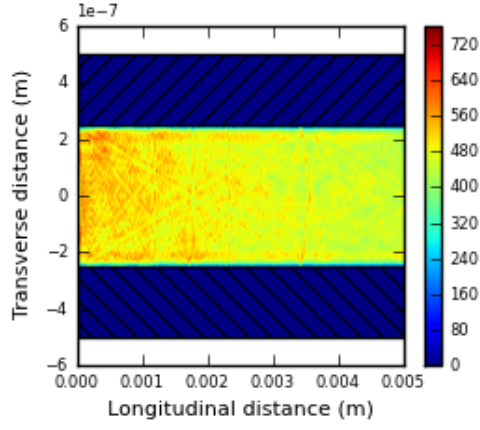
(c) Normal incidence, real source

(d) Incidence angle = 0.00015 rads, narrow source
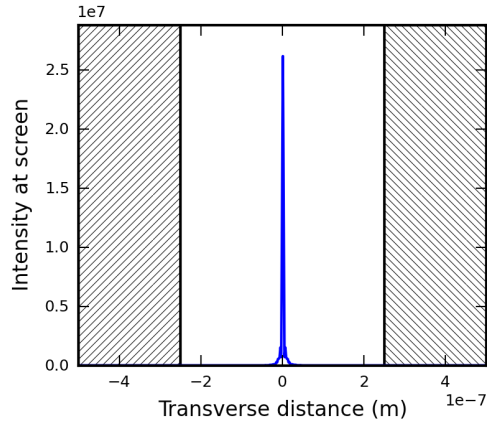

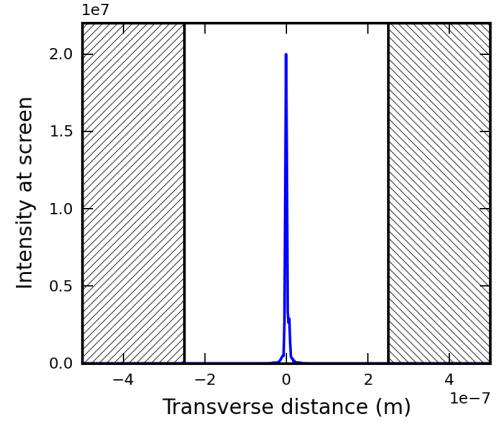(e) Incidence angle = 0.003 rads, narrow source

(f) Incidence angle = 0.003 rads, wide source

Figure 18: Results of the incoherent superposition simulation – computed intensity profiles for various sources and incidence angles.

(a) Normal incidence, polychromatic source

(b) Incidence angle = 0.00015 rads, polychromatic source

(c) Incidence angle = 0.0008 rads, polychromatic source

(d) Incidence angle = 0.003 rads, polychromatic source

(e) Incidence angle = 0.003 rads, narrow source

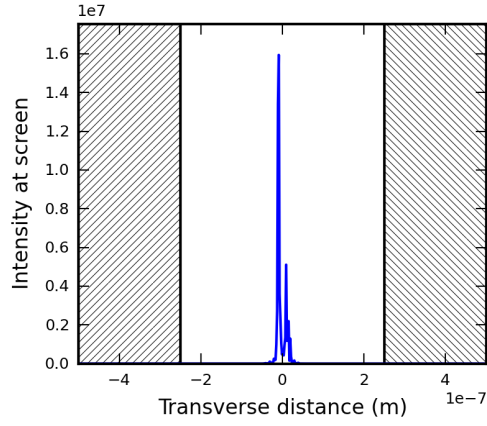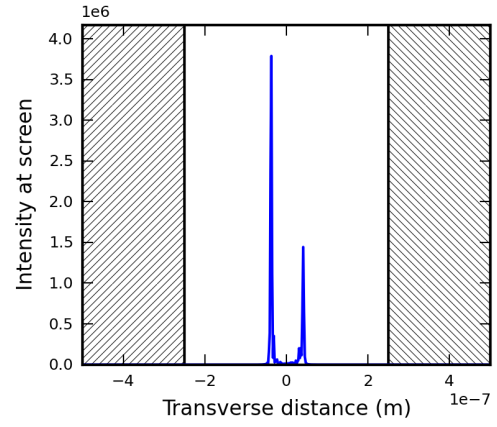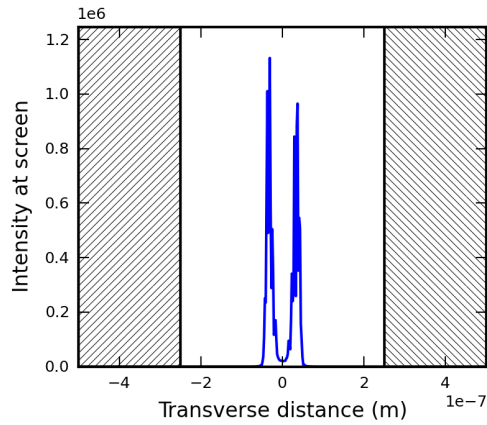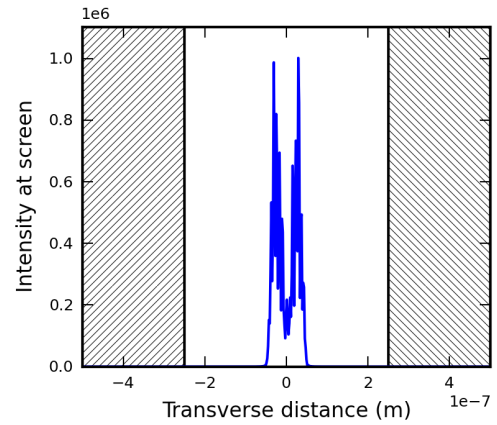(f) Incidence angle = 0.003 rads, wide source

Figure 19: Results of the incoherent superposition simulation – computed intensity profile at a screen placed far away from the waveguide exit.

There is another feature worth pointing out in a comparison between figures 18e and 18f. There appear to be more, and better defined, fringes in the narrow angular spread source case (figure 18e) compared to in the wide spread case (figure 18f). This makes good physical sense, since coherence really is the capacity of a field to form interference fringes, giving another validation of the model.

In contrast to the visible difference caused by changes in the spatial coherence, the wavelength spread of the X-ray source does not appear to have a large impact on the waveguide field. Figure 15a shows the intensity map for normal incidence plane waves that are totally coherent, and figure 18b shows such a map for a superposition of plane waves that have identical directions, but wavelengths that vary according to the distribution in figure 9. There are absolutely no visible differences between the two figures, indicating that, for the wavelength spread in a realistic lab X-ray source, temporal incoherence is not a major issue; only the spatial coherence is.

Figure 19 shows the simulation's computed intensity profile at a screen far downfield of the waveguide exit surface, again for selected combinations of source and incidence angle. The first four images, figures 19a to 19d, are for a source with no angular spread at increasing incidence angles. The form of these plots is two peaks, which get farther apart as the incidence angle is increased. Additionally, the left peak is significantly stronger than the right peak.

The two branches can be explained by considering that equation (14) gives the field inside the waveguide as a sum of two counter-propagating plane waves, each corresponding to a reflection off one waveguide slab. After the exit of the waveguide, these waves are no longer confined and are allowed to move in opposite directions freely. The higher the incidence angle on the waveguide, the greater the angle between these two plane waves inside the waveguide, and hence the farther they will spread out once they leave the waveguide. This gives rise to the two branches observed in figure 19.

This does not explain, however, why the left branch (presumably corresponding to the direction of the incident plane wave) is larger than the right branch. Some clues may be had by looking at the differences between figures 19d to 19f, which show the screen intensity for a 0.003 radian incidence angle and sources with a progressively increasing angular spread. It is seen that as the spatial coherence of the source is increased, the branches become less defined. This makes sense, because the spread of angles will give a spread of peaks a the screen. However, it is also seen that as the spatial coherence drops, the relative magnitude of the left and right peaks tends towards becoming the same. This effect cannot be explained by this argument alone.

3.4 Model Summary

The model developed in this project was based on the key idea of a wavefunction of the form of equation (13), and plane wave coupling into the waveguide based on equations (10) and (11). However, the model has predicted a number of effects that were not explicitly encoded into it. Many of these effects make good physical sense, providing a validation of the physics used in the model. Of particular interest are some effects which are not shown in previous models using a linear attenuation coefficient, such as the flow of energy in the transverse direction of the waveguide. However, the results of the model raise as many questions as they answer, and some predictions will need to be left to future work to explain.

4 Experimental

In addition to the modelling, which was the main thrust of this project, a simple experiment for validating some of the predictions of the model was performed. An X-ray waveguide was illuminated with a lab-based X-ray source and scanned over a range of incidence angles; a detector measured the resulting intensity far downfield of the waveguide. This experiment is described in this section, and a brief overview of the initial results are presented. Unfortunately, due to time constraints, a thorough analysis of the experimental results was not performed in this project.

4.1 Experimental Procedure

4.1.1 Source Characterisation

The first part of the experiment was to characterise the X-ray source. This was done by illuminating a silicon (400) crystal with the source, and recording the reflected intensity near the Bragg angle. The resulting X-ray intensity as a function of angle should then be the theoretical rocking curve convolved with the temporal and spatial spread of the source; this is illustrated in figure 20.
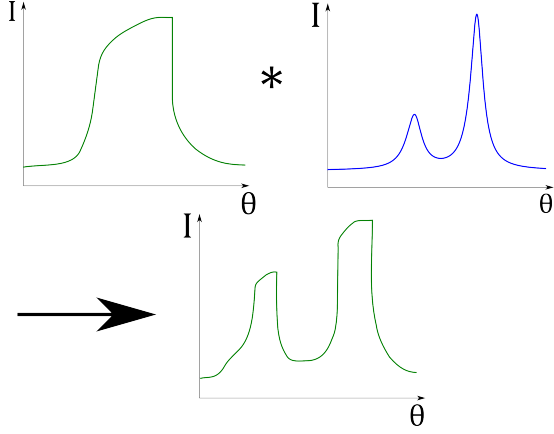
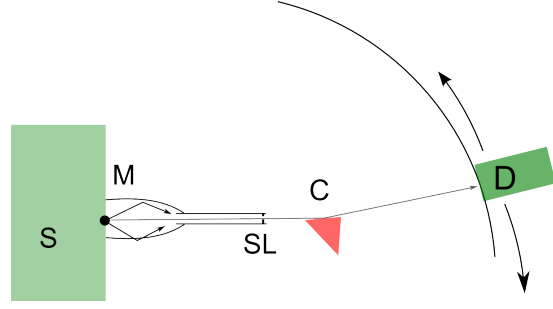Figure 20: The wavelength spread of the X-ray source causes the rocking curve to broaden and display two peaks

Figure 21: Experimental setup for the rocking curve measurement. The source S is collimated by the multilayer parabolic mirrors M. X-rays then pass through a slit SL to reflect off a silicon (400) crystal C. Photons are then detected at detector D as a function of angle.
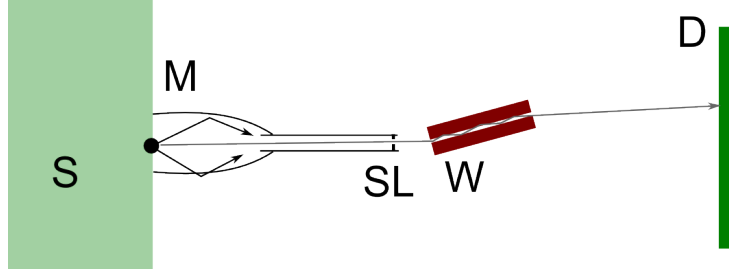

Figure 22: Experimental setup for the waveguide far-field measurements. The source S is collimated by the multilayer parabolic mirrors M. X-rays then pass through a slit SL, after which they are coupled into a waveguide W. The light field leaving the waveguide is measured at the far-field with a CCD detector D.

The experimental setup used to do this is shown in figure 21. The source is a rotating anode X-ray tube with a copper target, operating at 40 kV and 65 mA. The divergent X-rays from the source are collimated by a pair of multilayer parabolic mirrors, and then strike a silicon (400) crystal via a 350 μm slit (which ensure that the beam only strikes one crystal surface). A diffractometer was then used to measure the X-ray intensity over a range of $1000''$ around the Bragg angle.

4.1.2 Waveguide Measurements

A similar setup was used to illuminate the waveguide; this system is shown in figure 22. The source is again collimated by the mirrors, illuminating the waveguide via a 350 μm slit. The waveguide itself was mounted in the path of the beam, attached to a rotating table so that it could be scanned through an angular range. A stationary 2-D Medipix detector (pixel size 55 μm) was placed 65 cm from the waveguide.

The waveguide was scanned over an angular range of $1150''$ (5.5 mrad) either side of normal incidence, which is well beyond the critical angle (see figure 17). A step size of $8''$ was used, with each angle being illuminated for 5 minutes.

The Medipix detector was set up, independently of the angular scan, to continually acquire images with a 3 s exposure time. It was not possible using the equipment available to trigger the detector only when the angle was changed.

4.2 Results

Because the detector was not triggered by the rotating table, the data obtained from this experiment is correlated with the angular position of the waveguide only through the timing. The detector took an image every 3 s, and each angle was illuminated for 5 min; thus, at a first approximation, each block of 100 images represents the same angle and can be added together.

(a) Low incidence angle   (b) High incidence angle   (c) Very high incidence angle
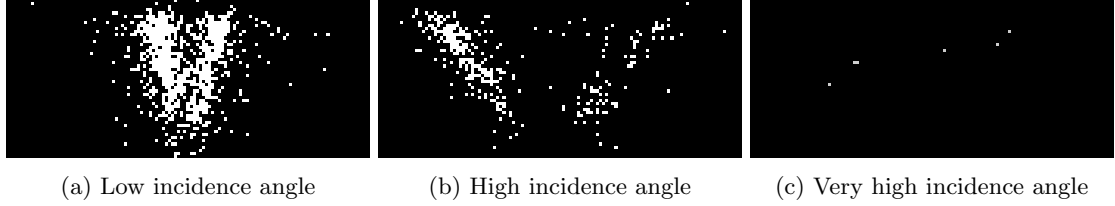
Figure 23: Three images acquired from the waveguide experiment, for a (a) low, (b) high, and (c) very high grazing angle. The two low images consist of two branches, which get farther apart in the higher one. The highest grazing angle is beyond the critical angle, and so the waveguide couples no intensity.

However, this does not take into account the lag between the detector acquiring frames, as well as the time taken to actually move the waveguide between angles. In reality, a number of pieces of information will need to be combined to get an accurate correlation between the detector images and the angle of illumination. This includes the timing, detecting sharp changes in between frames and detecting blurred frames (corresponding to the angle changing during frame acquisition). This work was not performed in this project, due to time constraints.

However, even without this correlation, some qualitative observations of the captured images can be made. A selection of representitive frames are shown in figure 23. The image with the highest grazing angle (figure 23c) has effectively no intensity recorded at the detector. This is because this angle is above the critical angle, meaning no intensity can be coupled into the waveguide.

The other two incidence angles (figure 23a and 23b) show two distinct branches of intensity. These branches are caused by reflections off the two waveguide walls, by the argument previously given for the simulation. The branches come closer together for the lower incidence angle; this is because the intensity is contained in low-order modes, which do not diverge as much (again, as explained in an earlier section).

Another feature of note is that the branches are in fact diagonal, and not straight. This is caused by an imperfection in the waveguide – the gap between the slabs is in fact not constant in the third dimension not considered so far in this project. The X-rays that couple into the part of the waveguide with a larger slab gap are contributing to the bottom part of the images in figure 23, and the X-rays that couple into the narrower part, into the upper region of figure 23. Each horizontal slice of the images in figure 23 can be considered as the intensity profile of a single 2-dimensional planar waveguide with a certain slab gap. The entire image can then be thought of as a stack of 2-dimensional waveguides next to each other, each contributing to a different horizontal line.

One final thing to note is that an inspection of figure 23b shows that the left branch contains visibly more intensity than the right branch. It is not clear whether or not this is the case for figure 23a; more images taken at this angle would need to be analysed to get a higher signal-to-noise ratio to see this.

5 Discussion

5.1 Comparison of Model to Experiment

The unprocessed images from the experiment conducted on the waveguide in figure 22 can be directly compared with the predictions of the model. Recall that figure 19 shows the simulated intensity in the far-field when the waveguide is illuminated under various conditions. This is precisely what is being measured in the experiment.

Many features of the experimental data are well explained by the model. Both the model results and the experimental data display the two branches of intensity. For the simulation, this was explained in section 3.3.3 as being due to the form of equation (14). The field inside the waveguide core is two plane waves propagating in opposite directions, so after the exit surface of the waveguide, there are effectively two rays moving in opposite directions.

Another feature of interest in the experimental data is that as the angle of illumination is increased, the branches get farther apart. This behaviour is also seen in the model. This happens because the higher the illumination angle of the waveguide, the higher the angle of the waves propagating inside the waveguide, and hence the faster they spread out outside the waveguide.

The simulation predicted that there would be a significant imbalance in the intensity carried by the two branches at the screen. This effect also appears to have been borne out by the experimental data – figure 23b in particular has more intensity on the left than on the right. This is believed to be because

of the choice of waveguide length. Consider the bouncing rays in figure 15d; if the waveguide ends in between two bounces, then the ray will be travelling predominately in one direction and so the intensity will be focused on one branch. If, however, the waveguide ends on a bounce, then there will be equal amounts of wave travelling in either direction, and hence the intensity will be equally distributed between both branches. This also explains why the branches become more even with increasing incoherence; the intensity becomes more smeared out over the waveguide and so there is not as strong a tendency for it all to travel in the same direction.

One thing that cannot be directly predicted from the model is the diagonal slant of the branches in the experiment. This is because the model is limited to two dimensions, and so cannot deal with the distribution of slab gaps in the real, slightly bent waveguide. The model therefore represents a horizontal slice through the experimental data. The model could, however, indirectly predict the slant in figure 22 if it was executed sequentially with different values for d. The collated results could be put into a 2-dimensional plot with the vertical axis being the waveguide slab gap, and the horizontal axis being the spatial coordinate of the detector. This might look like the experimental results – however, it would not take into account any interaction between waves in the vertical direction. A more sophisticated model would be needed to totally describe such a bent waveguide.

Overall, there appears to be excellent agreement between the model's predictions and a cursory examination of the results of experiment. Thus, it can be confidently said that, for a planar waveguide similar to the one discussed in this project, the model developed here contains all of the important physics. This model could be useful in the future because it could be used to predict several properties of interest for imaging applications of a planar waveguide. These might include the amount of intensity lost inside a waveguide of a certain length, and the coherence length of the radiation at a certain point outside the waveguide.

5.2   Talbot Carpets

One of the most unexpected results of the simulation was the prediction of Talbot carpets inside the waveguide. This effect has been discussed in [14] and [15] and is explained as being due to the formation of a "virtual grating". Each reflection from a ray on the waveguide walls can be traced back to a virtual source at the plane of incidence, giving a grating with a period of $2d$. The Talbot effect results in an image of the "grating" being re-formed periodically as the wave propagates with a certain characteristic period.

If it is considered that there is a phase shift on reflection of π, [15] gives the distance of these revivals as $\frac{d^2}{\lambda}$. This is in good agreement with the prediction for normal incidence of a coherent plane wave, shown in figure 15a. This figure shows the field at the waveguide entrance being recreated periodically as the field is propagated through in the z-direction. The predicted Talbot distance is slightly smaller than the observed distance (by 0.1 mm), most likely because in a dielectric, the phase shift on reflection is not exactly π.

One subtle effect in figure 15a is that every half-period, the field at the waveguide entrance is recreated, but at half the size. It is also just observable that every 1/3-period, the field is recreated at one-third the size. This effect is also observed in [15], and is of particular interest for imaging applications of waveguides. If the length of the waveguide is tuned so that it ends half-way through a Talbot period, the effective source size of the waveguide exit surface will be halved, with no loss of intensity. This means that the spatial coherence of a beam after travelling through the waveguide will be much improved.

When some degree of spatial incoherence is introduced into the source illuminating the waveguide, three things appear to occur. Firstly, the Talbot distance apparently doubles; this is seen best in figure 18d. This occurs because some symmetry is lost. At normal incidence, only even modes can be excited, however once the source is allowed to be incoherent, odd modes are also excited. This reduction in symmetry leads to a doubling of the Talbot distance.

Secondly, the Talbot effect becomes fractal in character. Where previously half-way to the Talbot distance a half-sized image of the entrance field was formed, now two such images are formed, one atop the other. The origin of this effect is unclear, but it seems likely it could be related to the Fourier shift theorem – phase shifting a wave by π is equivalent to translation by half a period. A more detailed analysis of the wave optics encoded in equation (10) will ultimately be needed to make this description precise.

Finally, because of the incoherent nature of the incident field, the Talbot effect becomes much less defined. In figures 18a, 18c and 18d, the entire waveguide is shaded predominantly yellow, with certain features of the Talbot effect coloured in green (slightly lower than yellow) (i.e. the intensity is similar

across the entire waveguide). This is in stark contrast to the coherent incidence case, where most of the waveguide is blue (almost no intensity). Thus, tuning the length of the waveguide would not have a dramatic effect on the effective source size the way it would for the coherent case. It may still have some effect – how much, exactly, would need to be determined by an analysis of the wavefield after the exit surface of the waveguide.

An inspection of figures 18e and 18f shows that the Talbot effect is either non-existent or much less pronounced for high grazing angles. This could be because the spacing of the angles for high-order modes is not as regular as for low order modes. This can be verified by an inspection of figure 7 – the shape of the red curve is flat for low grazing angles, leading to evenly spaced solutions for k_x, whereas for high angles, the solutions are not as evenly spaced. This would mean that the ray crossover points for the different modes are not well aligned, leading to a lack of a Talbot effect.

5.3   Future Work

The research in this project has raised more questions than it has answered! Here, some possible avenues for continuing this research are briefly discussed.

To enable further interrogation of the model, as a matter of convenience, its execution needs to be significantly sped up. At the moment, due to Python's Global Interpreter Lock (GIL) [17], the simulation is fundamentally single-threaded, and so gains no benefit from the multi-core CPU's common in today's computers. Certain performance-critical sections of the simulation need to be re-written in C++, which will both speed up single-thread performance and enable concurrent execution of parts of the simulation which are independent (for example, illumination by incoherent plane waves). This will make further interrogation of the model's predictions possible.

The model so far has not been used to make predictions about the coherence of radiation emerging from the waveguide's exit surface. This is really the objective of this research – to use waveguides as partially coherent sources in the lab. One way this prediction might be carried out is to simulate a test object (that changes the phase of waves passing through it) downfield of the waveguide. When the wavefield is numerically propagated through this object and onto a screen, the character of the resulting phase-contrast image could be used to determine how coherent the radiation is.

The experiment that was conducted in this project generated a lot of data that has not yet been analysed. Using the heuristics outlined in the results section, it would be possible to stitch the frames acquired with the detector in with the angular scanning of the waveguide to obtain definite angles of illumination for the images. Images that were taken at the same illumination angle can then be added together to boost the signal-to-noise ratio. The measurement of the silicon (400) rocking curve can be used to properly characterise the angular and wavelength spread of the source; these parameters can be fed into the simulation to simulate the true X-ray source used. This will allow *quantative* comparisons to be made with the simulation and the experiment, as well as a precise measurement of the waveguide's slab gap (and the degree to which this is bent).

The Talbot effect that is observed in the simulation could almost certainly be explained by a detailed analysis of the mode superposition expression in equation (10). One should in principle be able to obtain the conditions for total and fractional revival, as well as the transverse shift and demagnification present when the radiation is incoherent. This could be done by starting with equation (10), multiplying it by the propagator $e^{ik_z z}$ and finding the condition that the propagator gives a 2π phase shift to all mode wavefunctions.

6   Conclusion

The model developed in this project comprehensively describes a wide range of behaviour of an X-ray waveguide. The model takes loss into account naturally, which enables the model to show behaviour that cannot be predicted with previous analytical approaches – this behaviour includes an energy flow in the transverse direction due to loss in the cladding. It is also able to predict the observed 2-branch structure of far-field intensity, without any explicit encoding of such. Furthermore, it predicts the Talbot effect inside a planar waveguide, which becomes less pronounced when the X-ray source becomes less coherent. It is hoped that this model will be of use in the future for finding ways to increase the spatial coherence of X-ray sources using planar waveguides, enabling a wide range of coherent imaging techniques, such as phase-contrast, to be performed in the lab.

References

[1] Alexander McPherson. *Introduction to Macromolecular Crystallography*. John Wiley & Sons, New Jersey, 2nd edition, 2008.

[2] Shu-Ang Zhou and Anders Brahme. Development of phase-contrast x-ray imaging techniques and potential medical applications. *Physica Medica*, 24(3):129 – 148, 2008.

[3] Bahaa E. A. Saleh and Malvin C. Teich. *Fundamentals of Photonics*. John Wiley & Sons, 1991.

[4] B.L. Henke, E.M. Gullikson, and J.C. Davis. X-ray interactions: photoabsorption, scattering, transmission, and reflection at e=50-30000 ev, z=1-92. *Atomic Data and Nuclear Data Tables*, 54(2):181–342, July 1993.

[5] Christian Fuhse. *X-ray waveguides and waveguide-based lensless imaging*. PhD thesis, University of Goettingen, 2006.

[6] Eugene Hecht. *Optics*. Pearson Education, San Francisco, 4th edition, 2002.

[7] Christian Fuhse and Tim Salditt. Finite-difference field calculations for one-dimensionally confined x-ray waveguides. *Physica B: Condensed Matter*, 357(1-2):57 – 60, 2005.

[8] M. Deutsch, G. Hölzer, J. Härtwig, J. Wolf, M. Fritsch, and E. Förster. $K\ \alpha$ and $K\ \beta$ x-ray emission spectra of copper. *Phys. Rev. A*, 51:283–296, Jan 1995.

[9] Eric Jones, Travis Oliphant, Pearu Peterson, et al. SciPy: Open source scientific tools for Python. `http://www.scipy.org/`, 2001–.

[10] John D. Hunter. Matplotlib: A 2d graphics environment. *Computing In Science & Engineering*, 9(3):90–95, 2007. `http://matplotlib.org`.

[11] Richard P. Brent. *Algorithms for Minimization Without Derivatives*. Prentice-Hall, New Jersey, 1973.

[12] J. J. Moré, B. S. Garbow, and K. E. Hillstrom. User Guide for MINPACK-1. *ANL-80-74, Argonne National Laboratory*, 1980.

[13] J. A. Nelder and R. Mead. A simplex method for function minimization. *The Computer Journal*, 7(4):308–313, 1965.

[14] Yu.B Ovchinnikov. Revivals of light in a planar metal waveguide. *Optics Communications*, 182(1-3):35 – 43, 2000.

[15] Inna Bukreeva, Alessia Cedola, Andrea Sorrentino, Daniele Pelliccia, Viktor Asadchikov, and Stefano Lagomarsino. Resonance modes filtering in structured x-ray waveguides. *Opt. Lett.*, 36(14):2602–2604, Jul 2011.

[16] M Berry. Quantum carpets, carpets of light. *Physics World*, 14(6):39–44, 2001.

[17] Python Software Foundation. Python v2.7.3 documentation- python/c api reference manual. `http://docs.python.org/c-api/init.html`, 2012.